

MODELING HEAT AND MOISTURE TRANSPORT IN STEAM-CURED MORTAR: APPLICATION TO AASHTO TYPE VI BEAMS

E. Hernández-Bautista^{1,2*}, S. Sandoval-Torres¹, P. F. de J. Cano-Barrita¹, D. P. Bentz²

¹. Instituto Politécnico Nacional/CIIDIR Unidad Oaxaca, Hornos 1003, Oaxaca, México. C.P. 71230.

². National Institute of Standards and Technology, Gaithersburg, MD, USA.

*Corresponding author: ehernandezb0800@alumno.ipn.mx

Abstract

During steam curing of concrete, temperature and moisture gradients are developed, which are difficult to measure experimentally and can adversely affect the durability of concrete. In this research, a model of cement hydration coupled to moisture and heat transport was used to simulate the process of steam curing of mortars with water-to-cement (w/c) ratios by mass of 0.30 and 0.45, considering natural convection boundary conditions in mortar and concrete specimens of AASHTO Type VI beams. The primary variables of the model were moisture content, temperature, and degree of hydration. Moisture content profiles of mortar specimens (40 mm in diameter and 50 mm in height) were measured by magnetic resonance imaging. The degree of hydration was obtained by mass-based measurements of loss on ignition to 1000 °C. The results indicate that the model correctly simulates the moisture distribution and degree of hydration in mortar specimens. Application of the model to the steam curing of an AASHTO Type VI beam indicates temperature differences (between the surface and the center) higher than 20 °C during the cooling stage, and internal temperatures higher than 70 °C that may compromise the durability of the concrete.

Keywords: Mortar, steam curing, hydration, heat and mass transport, magnetic resonance imaging, AASTHO Type VI concrete beam

1. Introduction

Steam curing of concrete at atmospheric pressure has the advantage of accelerating the hydration reactions of Portland cement. Consequently, the material develops compressive strength and reduces its permeability in a shorter time compared with standard curing under ambient conditions. Under normal ambient conditions, depending on the type of cement and its fineness, the compressive strength can reach up to 50 % of the final strength in 3 d, and 80 % in 10 d [1]. Accelerated curing increases the strength gain at early ages, even though there is often a strength reduction at later ages compared to standard curing [2].

Cement hydration reactions are exothermic and the rate of reaction depends on the water-to-cement ratio (w/c), type of cement, and curing conditions. Heat generated by the hydration reactions contributes to the increase in temperature of the material. Temperature gradients that develop may have adverse effects on concrete durability. For instance, it has been reported that thermal gradients during hardening play an important role in the performance of joints in concrete pavements [3]. Krauss and Rogalla (1996) state that proper control of temperature may lead to reduced cracking in columns of bridges [4]. Temperature differences between the surface and the interior concrete higher than 20 °C may cause cracking, due to the magnitude of the coefficient of thermal expansion (CTE) of the concrete [4–6]. Also, an excessive increase in concrete temperature must be avoided during the heating phase in steam-cured concrete, as well the maintenance of moderate cooling ramps to prevent rapid changes in volume. During steam curing, the curing temperature should not be increased or decreased by more than 22 °C to 33 °C per hour, depending on the type of concrete, and the size and shape of the element [7], as well as on the preset time (the time delay prior to steam curing). It is also necessary to avoid concrete temperatures above 70 °C [8], as higher temperatures inhibit the formation of ettringite. At a later age and under certain conditions of temperature and humidity, a hardened concrete previously exposed to these higher temperatures may present delayed ettringite formation (DEF). If this occurs, the growing ettringite crystals may exert pressure on the surrounding cement paste causing it to crack [9].

On the other hand, at early ages, excessive water loss by evaporation at the concrete cover may cause an inadequate hydration and drying shrinkage cracking [10]. Hence, it is necessary to use alternative curing methods to ensure appropriate hydration. Moisture gradients inside

concrete during hydration may cause drying shrinkage due to the generation of capillary pressure in the pores, and with the restrictions exerted by aggregates and the reinforcing steel, cracking may occur. In order to predict these phenomena and determine curing conditions and mixture proportions that would avoid or minimize cracking, the aim of this work is to numerically simulate the moisture content, temperature, and degree of hydration during steam curing at atmospheric pressure of mortar specimens and in an AASHTO type VI beam with w/c of 0.30 and 0.45. The model previously developed by Hernández-Bautista et al. [11,12] is used as the basis and compared to experimental results obtained from nuclear magnetic resonance/magnetic resonance imaging (NMR), loss on ignition (LOI), and Fourier Transform Infrared (FTIR) spectroscopy tests.

2. Experimental procedure

2.1 Materials

2.1.1 Materials and specimen preparation

Portland cement with a chemical composition shown in Table 1, and silica sand with a fineness modulus of 2.9 and absorption of 2.56 % were used to prepare mortar mixtures. The mortar was considered as a model of concrete, as both contain cement, water, and aggregates. Two mixtures with w/c of 0.30 and 0.45 by mass (Table 2) were prepared according to the ASTM C305-06 standard [13]. The amount of silica sand in the mixtures represents 60 % of the mortar volume. Two mortar specimens measuring 40 mm in diameter and 50 mm in height were cast in glass containers (Figure 1a) for each w/c , to be subsequently analyzed using NMR. The containers were previously tested to verify that they did not contribute to the magnetic resonance signal.

2.2 Method

Once the specimens were cast, they were placed in an environmental chamber at 25 °C and covered with a wet cloth for 3 h (Figure 1b). The steam curing cycle inside the environmental chamber consisted of four stages: 1) a preset period prior to heating; 2) a heating ramp of 17.5 °C/h, for a period of 2 h, 3) a constant temperature at 60 °C for 10 h, and 4) a cooling period at a rate of 17.5 °C/h, for 2 h. This curing program was based on ACI 517-2R-80 for accelerated steam curing of concrete at atmospheric pressure [7]. In order to maintain a

relative humidity close to 100 % at a temperature of 60 °C inside the chamber, a steam generator was necessary. The relative humidity and the temperature inside the chamber were recorded with a thermo-hygrometer with a range of 0 % to 100 % relative humidity with an accuracy of ± 2.5 %.

Because the temperature and relative humidity of the air inside the curing chamber were controlled and there was no forced convection, it was considered that heat transfer was by natural convection. Mass transfer coefficients were therefore small and were calculated using experimental data. During curing, the specimens were removed from the environmental chamber every 2 h to perform NMR measurements. These measurements were undertaken using an Oxford Instruments DRX-HF 12/50 spectrometer operating at a frequency of 12.9 MHz (Oxford Instruments Ltd, Abingdon, Oxford, UK)¹. The selective population inversion (SPI) [14] and the Carr-Purcell-Meiboom-Gill (CPMG) [15] techniques were used to obtain the evaporable water distribution and the pore size distribution changes during curing, respectively.

In addition, mortar samples of various ages were ground in the presence of ethanol to stop hydration and the powder was oven-dried at a temperature of 105 °C for 24 h. Powder samples were used to estimate the degree of hydration by the mass-based LOI technique, firing the dry powder to 1000 °C [8]. The degree of hydration is then estimated based on the non-evaporable water content determined from the LOI measurement. With the purpose of characterizing the progress of cement hydration, powder samples were also analyzed by FTIR spectroscopy to identify the main functional groups and their corresponding peak intensities. The functional groups characteristic of hydrated cement and their intensities were identified.

3. Hydration model

Equation (1) shows the generalized conservation equation. The components of the specific system of equations solved in the current study are shown in Table 3. The model consists of

¹ Certain commercial products are identified in this paper to specify the materials used and the procedures employed. In no case does such identification imply endorsement or recommendation by the National Institute of Standards and Technology, nor does it indicate that the products are necessarily the best available for the purpose.

two ordinary differential equations that describe the equivalent time and the degree of maturity of the material (Equations 2 and 3) [11,16]. The maturity equation (Equation 3), is obtained by derivation using the chain rule; the divergence term is zero. In addition, two partial differential equations were written, one for heat transfer and the other for moisture transport in the mortar (Equations 4 and 5 in Table 3).

$$e \frac{\partial U}{\partial t} = \nabla \cdot \mathbf{J} + Q \quad (1)$$

The source and sink terms (Q) in Equations 4 and 5 in Table 3 correspond to the generation of heat and the consumption of water, respectively, due to the exothermic hydration reactions. The Q term in equation 4, is similar to the degree of hydration, but multiplied by the ultimate heat of hydration (estimated from the potential Bogue phase composition of the cement). The following hydration reactions consume a majority of the mixing water: alite or tricalcium silicate (0.24 g/g cement), belite or dicalcium silicate (0.21 g/g cement) and tricalcium aluminate (0.40 g/g cement) [17] and at the same time they release heats of 535 kJ/kg cement, 262 kJ/kg cement, and 1146 kJ/kg cement, respectively [18], as they are all exothermic reactions. The water consumption term is the derivative of the hydration level multiplied by w_n , which is the amount of (non-evaporable) water per gram of cement needed for hydration [19]. The boundary conditions are globally expressed by Equation (6) and for each conservation equation they are presented in Table 4. Initial conditions represent the condition of the material at time $t = 0$ (Table 4). In the case of the initial conditions for the mass conservation equation (Equation 10), there are two possible initial conditions, since the water content in the specimen at the beginning depends on w/c . To complete the system of equations, variables and constitutive equations are presented for both w/c in Table 5 based on values taken from the literature for cement pastes and mortars similar to the ones studied here [20,21].

$$-\mathbf{n} \times \mathbf{J} = g \quad (6)$$

The system of equations was solved using COMSOL Multiphysics 4.4,¹ with a relative tolerance of 0.01 and a time step of 6 min. The modeled geometry consisted of 551 elements and 8686 degrees of freedom.

3.1 Simulation of hydration and heat and mass transport in an AASHTO type VI beam

The model was further employed to simulate steam curing of an AASHTO type VI beam (Figure 2a) to evaluate the temperature and moisture gradients in the cross section of the beam. The height of the beam is 183 cm and the top and bottom widths are 107 cm and 71 cm, respectively. The model couples the transport equations to the chemical reaction of hydration (maturity equation) for a 2D geometry. The curing process was simulated for the curing cycle described in section 2.2, with a 10 h period of constant temperature at 60 °C (Figure 2b).

4 Results and discussion

4.1 Comparison of experimental and simulated results

A 2D symmetric geometry was first used that represents mortar specimens cast in glass containers (Figure 1a), which were subjected to the steam curing cycle described in section 2.2. Table 4 shows the boundary conditions used in the simulations, which are mainly heat and mass transfer by convection at the surface.

The CPMG transverse magnetization decay (M_{xy}) was fitted to Equation 14 to obtain the short ($T_{2,1}$) and long ($T_{2,2}$) lifetime components and their corresponding signal intensities ($M_{0,1}$ and $M_{0,2}$) for the mortar samples. The intensities of the NMR signals were converted to moisture content by taking into consideration the initial moisture content (calculated from the mortar mixture proportions) and the final moisture content obtained by gravimetric measurements of oven-dried specimens. Uncertainties in the estimation of the moisture content by NMR are about 4 % [22].

$$M_{xy} = M_{0,1}e^{\frac{-t}{T_{2,1}}} + M_{0,2}e^{\frac{-t}{T_{2,2}}} \quad (14)$$

Figure 3 shows the simulated and experimental moisture contents during steam curing. The pattern evolution of the signal (decrease of moisture content) in the samples is mainly explained by water consumption due to the ongoing hydration reactions. During the steam curing experiments, no mass loss/gain was observed in the specimens. The decreasing moisture content patterns from NMR are explained by the chemical reactions (hydration). In

the mortar samples, there is no moisture absorption because the chemical potentials in the material and in the surrounding environment are similar [17]. A high environmental vapor pressure was provided by using a steam generator that was logged during the curing process.

The relaxation rate $1/T_2$ is related to the surface-to-volume ratio (S/V) of the pore system [23]. A decrease in T_2 implies an increase in the S/V ratio caused by pore refinement as the hydration products are generated. As shown in Figure 4a, the short $T_{2,1}$ lifetime components for mortar with a $w/c = 0.45$ are higher than those for the mortar with $w/c = 0.30$, as expected, due to the finer porosity of the latter. In both cases, after 3 h there is a significant reduction in T_2 values, indicating that the cement is hydrating and the sizes of the capillary pores are reducing significantly.

On the other hand, the long $T_{2,2}$ lifetime component (Figure 4b) is similar in both mortars after casting the specimens and by 3 h, it has decreased noticeably. After 3 h, the $T_{2,2}$ for the sample with $w/c = 0.45$ remains fairly constant. In contrast, the $T_{2,2}$ for the sample with $w/c = 0.30$ increases. This behavior may indicate micro-cracking caused by expansion of the air inside the mortar due to its temperature increase, and/or self-desiccation, which is expected to be more significant for the low w/c mortar [24]. It is important to consider that after 3 h of curing, the $T_{2,2}$ long lifetime component contributes less than 4 % to the total NMR signal. Therefore, it is the short $T_{2,1}$ lifetime component that mainly describes the microstructural changes in the mortars.

Figure 5 shows the experimental (symbols) and the simulated (lines) moisture profiles, which indicate a more or less homogeneous moisture distribution within the sample (along the z axis). However, in both mortars ($w/c = 0.30$ and $w/c = 0.45$) in the last hours, there is a decrease in moisture content in the end far from the face in contact with the steam. There is a reasonable agreement between the measured and the simulated data during the 18 h of the curing process. Estimation of the heat and moisture transport coefficients was based on a natural convection process occurring at the surface of the sample. This is because there was no forced convection in the chamber, and also the chemical reactions produce a temperature increase throughout the specimen, including at the surface. When this surface interacts with the water vapor, it makes the damp air experience density variations (buoyancy). For these

conditions, the Rayleigh, Grashof and Prandtl numbers were used to estimate the appropriate transfer coefficients (Table 5).

Table 6 shows the functional groups common in hydrated cement paste and their associated characteristic FTIR wavelengths [19]. The main functional groups identified were those belonging to the Si-O and Si-OH of the calcium silicate hydrate gel (C-S-H) at the 965 cm^{-1} band, and the hydroxyl group -OH of the calcium hydroxide (CH) at the 3641 cm^{-1} band. The intensities of these peaks increased during the curing process as a result of hydration. The anhydrous phases were not identified, since most of them exhibit peaks between 300 cm^{-1} and 800 cm^{-1} . The C-O functional group of calcium carbonate produces bands at 1418 cm^{-1} and 873 cm^{-1} [25,26]. Figure 6 shows the peak intensities for C-S-H and CH at different times. These intensities were measured by considering a baseline at time zero. The kinetics obtained are shown in Figure 7. As expected, the amounts of C-S-H and CH increase as the curing time increases. Although the information is valuable, it was not possible to compare it directly with the model, as the latter predicts the degree of hydration and not the concentration evolution of each individual phase. However, the intensity changes do reveal the generation of the main hydration products in the mortars and thus the expected trend in the degree of hydration. Therefore, these curves have a similar behavior/evolution as those for the hydration process as determined by the degree of hydration by LOI.

The degree of hydration by LOI can be compared with the degree of hydration obtained by numerical simulation, via the maturity equation (Equation 3). Figure 8 compares the simulated degree of hydration with the experimental values, with an excellent agreement. The degree of hydration will continue to increase beyond 16 h to 18 h. A higher degree of hydration in samples with w/c of 0.45 is obtained in comparison to the $w/c = 0.30$ mortar, as expected due to the increased availability of curing water in the former.

4.2 Simulation of heat and mass transport during hydration in an AASHTO Type VI beam

The heat generated by hydration reactions allows identification of the regions where the reactions take place with higher/lower intensity. Figure 9 shows simulated temperature distributions at different times during the curing process. During the first hours (5 h), the

temperature increases near the surface due to the steam curing and hydration reactions. At the beginning of the process, the material contains its maximum amount of water, which will decrease as hydration progresses. Also, the material has its highest heat capacity (Equation 12), and thus requires more energy to increase its temperature. The temperature rise is due to the following: 1) steam curing cycle in the chamber and 2) exothermic hydration reactions.

As a result, the slope in the evolution of surface temperature during the heating cycle will be much higher than the slope in the cooling period. The surface eventually reaches a higher temperature than the curing chamber due to heat released from the chemical reactions augmenting that supplied by the steam curing (Fig. 10). After the warming-up period, a constant temperature condition is imposed. Figure 10 shows a convergence point where internal and surface temperatures are the same, due to the increased heat generated by reactions inside the mortar (red dots in Figure 2). At this point, the surface reaches a high degree of hydration, and the internal points will eventually reach the same level, but with a time delay. After this stage, where temperatures are the same, the surface temperatures will be lower than the internal temperatures due to a relative decrease in the intensity of the hydration reactions (11 h) and the convective heat transfer occurring at the surface. As shown in Figure 10, at 11 h, the interior of the beams will be approximately 12 °C higher than the surface temperature.

Next, we consider two points away from the surface where there may be a higher difference in temperature and moisture content. For example, in Figure 10 at $t = 11$ h, there is a temperature gradient between the center and the surface of the material. The figure also shows the temperature history in these points, as well as the degree of hydration for the two mortars studied. It is observed that the interior and surface temperatures exceed the temperature of the environmental chamber by nearly 16 °C. This excess is observed after 6 h of the curing process. This point is important because the temperature increase is a restriction when curing concrete components of this type on an industrial scale, especially when it is required to avoid cracking and damage due to temperature gradients, which could have a negative impact on long term durability. In addition, it is also observed that the degree of hydration of the beam achieves a value of 0.40 for the $w/c = 0.30$ mortar. As expected, the degree of hydration for the mortar with $w/c = 0.45$ is higher ($\alpha = 0.52$) compared with that

of the mortar with $w/c = 0.30$, as a result of the limited water content in the latter. For the $w/c = 0.45$ mortar, the increase in temperature is even higher and the maximum temperature is obtained approximately at 11 h of the curing process. In this case, the difference in temperature between the chamber curing conditions and the interior of the material is approximately 19 °C. It is observed that curing at 60 °C and increasing w/c , the cooling process will be delayed. The temperature gradient is larger when w/c is greater, according to the simulations.

Figure 11 shows the estimated moisture distribution profiles along the height of the beam (red line in Figure 2a). It is observed that for both w/c , during the first hours of curing, the moisture distribution profiles are constant along the height. At 4 h of curing, there is a slight decrease in moisture content at the surface of the beam due to hydration reactions that consume evaporable water. At 6 h, this decreased moisture content at the surface is more evident. The model predicts a drying front at both ends (top and bottom of the beam), in spite of the high relative humidity conditions ($\approx 100\%$). At 12 h and 10 h of the curing process, there is a receding drying front approximately 1 cm deep for the $w/c = 0.30$ and $w/c = 0.45$ mortars, respectively. In the beam with $w/c = 0.45$, this happens sooner because of its higher water vapor diffusion coefficient [27]. During the cooling period for the beam with $w/c = 0.45$, an increased moisture content is observed at the ends, probably due to water condensation.

Figure 12 highlights the main practical results of this work for both w/c . In both cases, the maximum temperature reached within the specimens is higher than 70 °C, so it is possible that ettringite will become unstable and delayed ettringite formation could subsequently be an issue [9]. For the constant temperature curing period, it is observed that there are differences in temperature less than 12 °C (between the center and the surface of the beam), which are within the recommended limits [5,6]. However, in the cooling period, there are temperature differences that exceed 20 °C (but that could perhaps be reduced with a different curing cycle). The degree of hydration is greater for the mortar with $w/c = 0.45$ due to its higher availability of evaporable water for continuing the hydration reactions. In general, the achieved degree of hydration depends on the type of cement, w/c , water availability during curing, and curing temperature. In accordance with the simulations, some strategies that

could be applied to decrease temperature gradients are: 1) lower the curing temperature to 50 °C or even 40 °C, 2) increase the length of the constant temperature period, and/or 3) reduce the cooling rate 15 °C/h or less.

Based on the results, the developed model is able to predict the temperature evolution and moisture distribution, and the degree of hydration in the simulated beams. This model is an abstraction of the real system and process. Nevertheless, it can serve as an important tool for engineers, scientists and practitioners in the concrete industry to understand the important transport phenomena using mathematical equations. Thus, the model could be useful for design and scale-up, optimization, mechanistic understanding, evaluation/planning of experiments, determining quantities that cannot be measured directly, and realistic simulation of experiments that would be (too) costly to perform in the laboratory.

5 Conclusions

A previously developed mathematical model was applied to predict the mass and heat transport coupled to chemical reactions in small mortar specimens and in an AASHTO Type VI beam. For the small mortar specimens, the simulations were compared with experimental data for two water/cement ratios ($w/c = 0.30$ and $w/c = 0.45$). The main conclusions are as follows:

The model correctly characterizes the moisture distribution in the mortar samples due to water consumption by hydration reactions, as compared with the experimental moisture content determined by NMR. The moisture distribution pattern is nearly homogeneous over time, but a small evaporative process was identified in the cooling period.

The FTIR results allowed estimation of the hydration kinetics for the two main hydration products, CH and C-S-H. The pattern of the normalized peaks, representing the formation of these products during hydration, shows an evolution similar to the experimental and simulated degree of hydration (based on LOI) curves.

The results of the simulation of an AASTHO Type VI beam indicate a maximum temperature difference of 12 °C in the period of constant temperature, between the center and the surface of the beam. Using a rate of change of temperature of 17.5 °C/h during the cooling period, a

maximum temperature difference of 26 °C is observed, which could cause cracking. For the same conditions of curing, but for a beam with $w/c = 0.45$, the internal temperature reaches 79 °C ($w/c = 0.30$ mortar reaches 76 °C), indicating that the beam potentially can be damaged by delayed ettringite formation, for example.

The moisture content profiles in the beams are generally homogeneous due to the applied curing conditions. There is effectively no drying during the process, but there is water consumption due to the hydration reactions. A change in the diffusion coefficient of the fluid with curing time was observed, especially in the $w/c = 0.45$ system.

These simulations provide the means to evaluate curing cycle changes, since their predictions are applicable to any geometry and water/cement ratio, provided that the required parameters in the maturity model and specifics of the curing conditions are known and used as inputs.

Acknowledgments

E. Hernandez-Bautista acknowledges NIST and the staff of their Materials and Structural Systems Division, Conacyt for the PhD scholarship and the Instituto Politecnico Nacional for the BEIFI scholarship. P. Cano acknowledges Conacyt of Mexico for funding the project with ID code 239727. S. Sandoval acknowledges SIP from IPN for funding the projects with ID codes 20144660 and 20161016.

Nomenclature

a Parameter for vapor diffusion coefficient $\text{kg}/(\text{m}\cdot\text{s})$

b Parameter for the liquid diffusion coefficient

c Parameter for the liquid diffusion coefficient

C_p^{CemBM} Cement-based material specific heat capacity $\text{J}/(\text{kg}\cdot\text{K})$

C_{pi} Specific heat capacity of the material i J/(kg·K)
 D_l Liquid moisture diffusion coefficient m^2/s
 D_v Vapor diffusion coefficient kg/(m·s)
 e Damping or mass coefficient
 E Activation energy J/mol
 H Total enthalpy of hydration J/kg
 H_u Ultimate enthalpy of hydration J/kg
 h_c Convective heat transfer coefficient W/(m²·K)
 h_m Mass transfer coefficient g/(m²·h·Pa) or s/m
 i Index for type of material
 J Conservative flux (mass or heat)
 k_i Thermal conductivity of material i W/(m·K)
 M_f^{water} Water mass fraction
 $M_f^{Boundwater}$ Bound water mass fraction
 M_f^{cem} Cement mass fraction
 $M_f^{silicasand}$ Aggregate mass fraction
 \mathbf{n} Normal vector
 P_{vext} Vapor pressure in the surroundings Pa
 P_v Vapor pressure inside the material Pa
 Q Heat generation rate W/m³ or Evaporable water sink kg/(m³·s)
 R Ideal gas constant, 8.314 J/(mol·K)
 t Time s
 T_r Reference temperature K
 T Temperature K
 t_e Equivalent time
 U Dependent variable

w Moisture content

Greek symbols

α Degree of hydration

α_u Ultimate degree of hydration

β Maturity equation parameter

λ_{vap} Heat of vaporization J/kg

ρ_i Density of material i kg/m³

ρ_s Density of the solid cement-based material kg/m³

τ Maturity equation parameter s

References

- [1] J.G. Wilson, N.K. Gupta, Equipment for the investigation of the accelerated curing of concrete using direct electrical conduction, *Measurement*. 35 (2004) 243–250. doi:10.1016/j.measurement.2003.11.002.
- [2] N.. Carino, H.. Lew, Temperature Effects on Strength-Maturity Relations of Mortar, *ACI Mater. J.* 80 (1983) 177–182.
- [3] H. Yu, L. Khazanovich, M. Darter, A. Ardani, Analysis of Concrete Pavement Responses to Temperature and Wheel Loads Measured from Instrumented Slabs, *Transp. Res. Rec. J. Transp. Res. Board.* 1639 (1998) 94–101. doi:10.3141/1639-10.
- [4] P.D. Krauss, E.. Rogalla, Transverse Cracking in Newly Constructed Bridge Decks, National Cooperative Highway Research Program (NCHRP, 1996.
- [5] A.M. Neville, *Properties of Concrete*, 5th ed., USA, 2012.
- [6] A.K. Schindler, Temperature Control During Construction to Improve the Long Term Performance of Portland Cement Concrete Pavements, Texas Department of Transportation, 2002.
- [7] American Concrete Institute, ACI 517-2R-80 Accelerated Curing of Concrete at Atmospheric Pressure, *ACI J.* (1980) 429–448.
- [8] S.H. Kosmatka, B. Kerkhoff, W.C. Panarese, Design and Control Design and Control of Concrete Mixtures, Fourteenth, Portland Cement Association, 2003.
- [9] Z. Zhang, J. Olek, Studies on delayed ettringite formation in heat-cured mortars II. Characteristics of cement that may be susceptible to DEF, *Cem. Concr. Res.* 32 (2002) 1737–1742.
- [10] P.K. Mehta, P.J.M. Monteiro, *Concrete Microstructure, properties, and Materials*, Third Edit, New York, USA, 2006.
- [11] E. Hernandez-Bautista, D.P. Bentz, S. Sandoval-Torres, P.F. de J. Cano-Barrita, Numerical simulation of heat and mass transport during hydration of Portland cement mortar in semi-adiabatic and steam curing conditions, *Cem. Concr. Compos.* (2015). doi:10.1016/j.cemconcomp.2015.10.014.
- [12] E. Hernández-Bautista, Transferencia de masa y calor con reacción química en materiales base cemento durante el curado con vapor de agua, Instituto Politécnico Nacional, 2016.
- [13] ASTM, Standard Practice for Mechanical Mixing of Hydraulic Cement Pastes and Mortars of Plastic Consistency, *ASTM Int. C305-6* (2010) 6–8. doi:10.1520/C0305-06.2.
- [14] S. Emid, J.H.N. Creighton, High Resolution NMR Imaging in solids, *Physica.* 128B (1985) 81–83.
- [15] S. Meiboom, D. Gill, Modified Spin- Echo Method for Measuring Nuclear Relaxation Times, *Rev. Sci. Instrum.* 29 (1958) 688–91.
- [16] E. Hernández-Bautista, S. Sandoval-Torres, D.P. Bentz, P.F. de J. Cano Barrita, Modeling Heat and Moisture Transport During Hydration of Cement-Based Materials in Semi-Adiabatic Conditions, in: *COMSOL Conf. Bost.*, 2014: pp. 1–5.

https://www.comsol.com/paper/download/194143/hernandezbautista_paper.pdf.

- [17] C. Hua, P. Acker, A. Ehrlacher, Analyses and model of the autogenous shrinkage of hardening cement paste. I. Modeling at macroscopic scale, *Cem. Concr. Res.* 25 (1995) 1457–1468.
- [18] D.P. Bentz, V. Waller, F. de Larrard, Prediction of Adiabatic Temperature Rise in Conventional and High-Performance Concretes Using A 3-D Microstructural Model, *Cem. Concr. Res.* 28 (1998) 285–297. doi:10.1016/S0008-8846(97)00264-0.
- [19] C. Hua, A. Ehrlacher, P. Acker, Analyses and model of the autogenous shrinkage of hardening cement paste. II Modelling at scale of hydrating grains, *Cem. Concr. Res.* 27 (1997) 245–258.
- [20] B. Villmann, V. Slowik, F.H. Wittmann, P. Vontobel, J. Hovind, Time-dependent Moisture Distribution in Drying Cement Mortars. Results of Neutron Radiography and Inverse Analysis of Drying Tests Determination of Moisture Transport Parameters and Moisture Profiles by Inverse Analysis, 20 (2014) 49–62. doi:10.12900/RBM14.20.1-0004.
- [21] D.P. Bentz, Transient plane source measurements of the thermal properties of hydrating cement pastes, *Mater. Struct.* 40 (2007) 1073–1080. doi:10.1617/s11527-006-9206-9.
- [22] P.F. de J. Cano-BarritaB., J. Balcom, T.W. Bremner, M.B. MacMillan, W.S. Langley, Moisture distribution in drying ordinary and high performance concrete cured in a simulated hot dry climate, *Mater Struct.* 37 (2004) 522–531.
- [23] G.R. Coates, L. Xiao, M.G. Prammer, *NMR Logging principles & applications*, Halliburton Energy Services, Houston, Texas, USA, 1999.
- [24] B. Persson, Self-Desiccation and Its Importance in Concrete Technology, *Mater. Struct.* 30 (1997) 293–305.
- [25] M. Chollet, M. Horgnies, Analyses of the surfaces of concrete by Raman and FT-IR spectroscopies: comparative study of hardened samples after demoulding and after organic post-treatment, *Surf. Interface Anal.* 43 (2011) 714–725. doi:10.1002/sia.3548.
- [26] R. Ylmén, U. Jäglid, B.M. Steenari, I. Panas, Early hydration and setting of Portland cement monitored by IR, SEM and Vicat techniques, *Cem. Concr. Res.* 39 (2009) 433–439. doi:10.1016/j.cemconres.2009.01.017.
- [27] M. Krus, *Feuchtetransport- und Speicherko effizienten poröser mineralischer Baustoffe.*, Universität Stutt, 1995.

Figure captions

Figure 1. a) Mortar specimens for the NMR measurements and b) experimental setup inside the environmental chamber for steam curing.

Figure 2. a) AASHTO Type VI beam geometry and b) Steam curing cycle.

Figure 3. Average moisture content in mortar specimens subjected to steam curing versus curing time. The MRI moisture content was obtained from the moisture distribution profiles and the NMR moisture content was obtained from the signal intensity of bulk CPMG measurements.

Figure 4. Transverse relaxation time T_2 versus curing time a) Short $T_{2,1}$ lifetime component, and b) Long $T_{2,2}$ lifetime component. Sample error bars indicate one standard deviation.

Figure 5. 1D Moisture content profiles of mortars at different steam curing times with maximum constant temperature of 60 °C a) $w/c = 0.30$ and b) $w/c = 0.45$. The experimental profiles were obtained by the SPI MRI technique.

Figure 6. FTIR spectra at different times during the curing process at 60 °C a) $w/c = 0.30$, b) $w/c = 0.45$

Figure 7. Normalized FTIR signal intensity of calcium silicate hydrate gel and calcium hydroxide peaks during steam curing versus curing time.

Figure 8. Simulated and experimental degree of hydration versus time during steam curing of mortar. The error bars indicate one standard deviation.

Figure 9. 2D interior temperature development (°C) at different times of an AASHTO type VI concrete beam during steam curing, a) $w/c = 0.30$ and b) $w/c = 0.45$

Figure 10. Interior temperature evolution and degree of hydration as a function of time in an AASHTO Type VI beam during steam curing, a) $w/c = 0.30$ and b) $w/c = 0.45$.

Figure 11. 1D moisture distribution along the vertical axis of an AASHTO Type VI beam during steam curing, a) $w/c = 0.30$) and (b) $w/c = 0.45$.

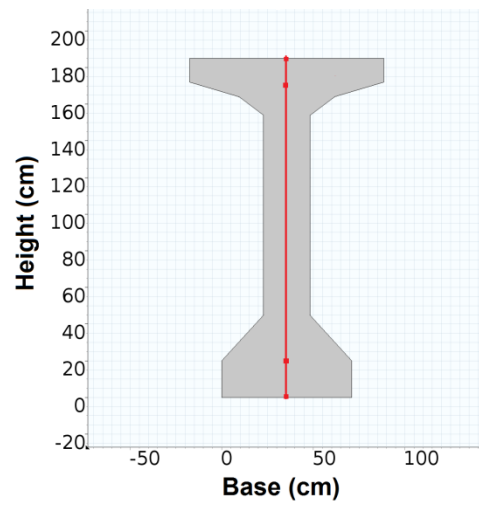
Figure 12. Simulated temperature and degree of hydration during steam curing of an AASHTO Type VI beam. The steam curing cycle considered is shown in Figure 2. The difference in temperature concerns two locations: the center and the surface of the beam.



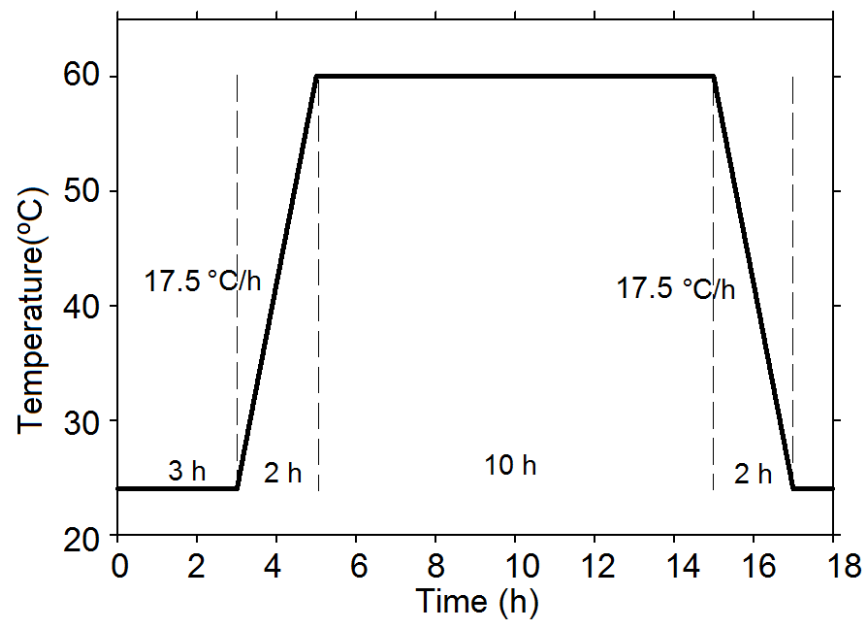
a)

b)

Figure 1



a)



b)

Figure 2

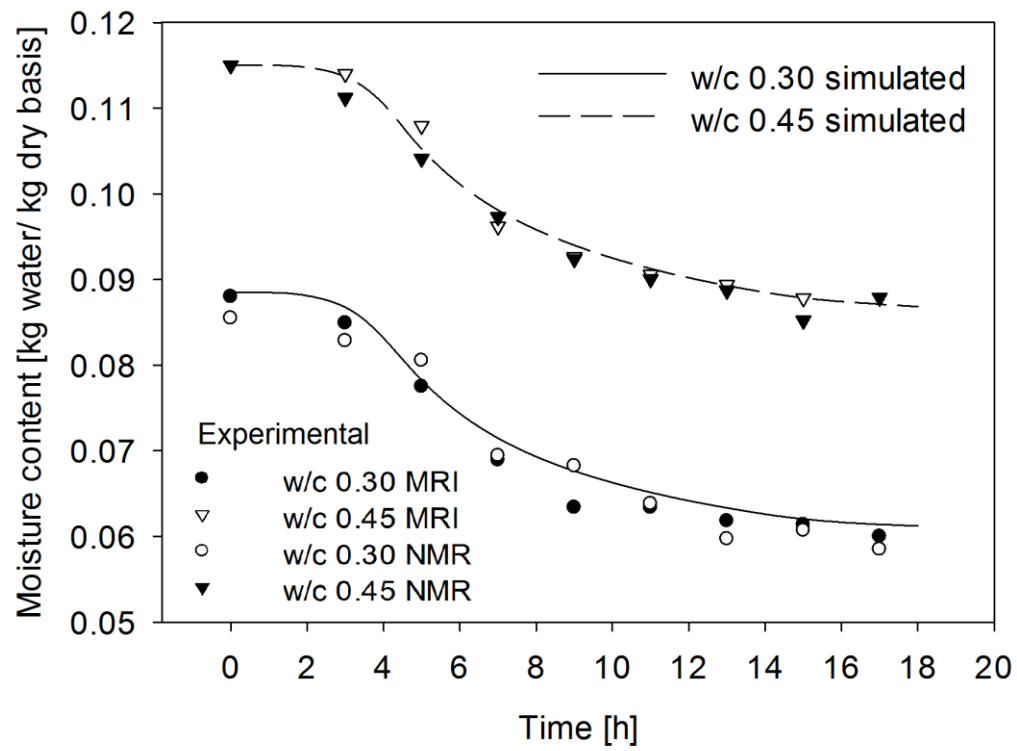
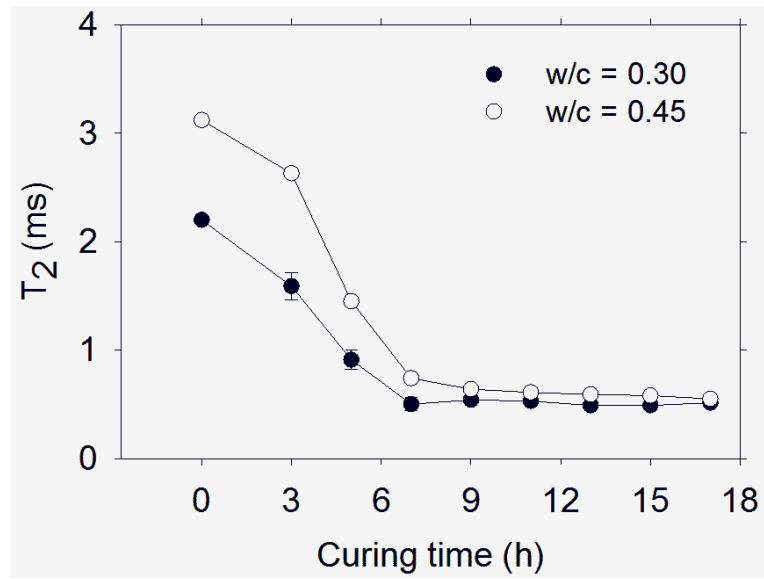
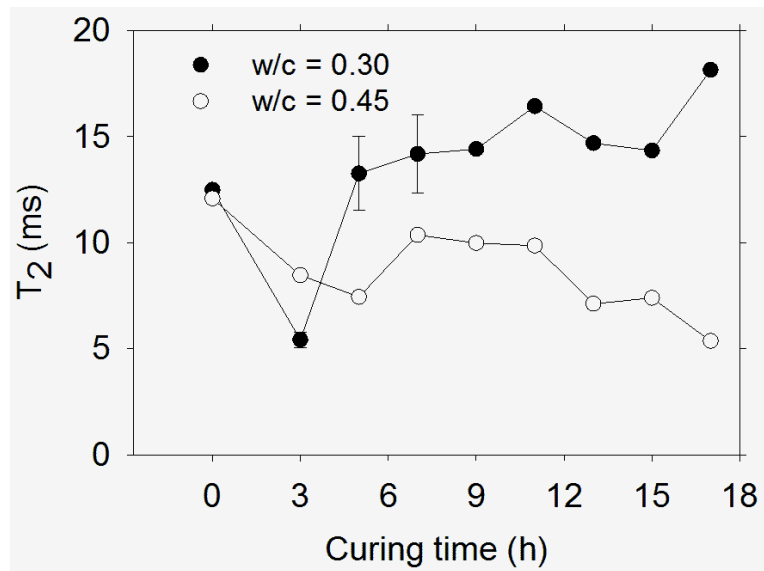


Figure 3

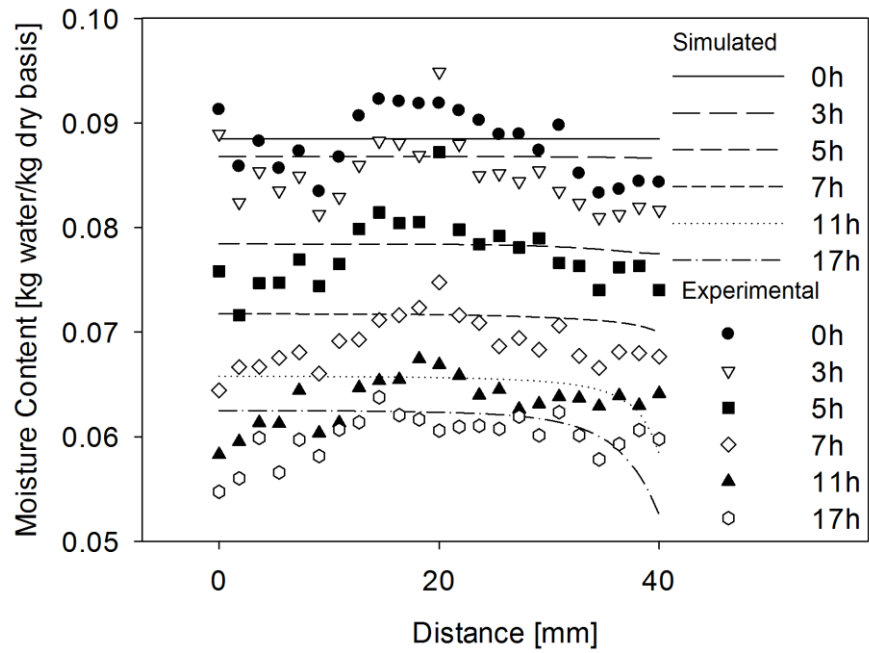


a)

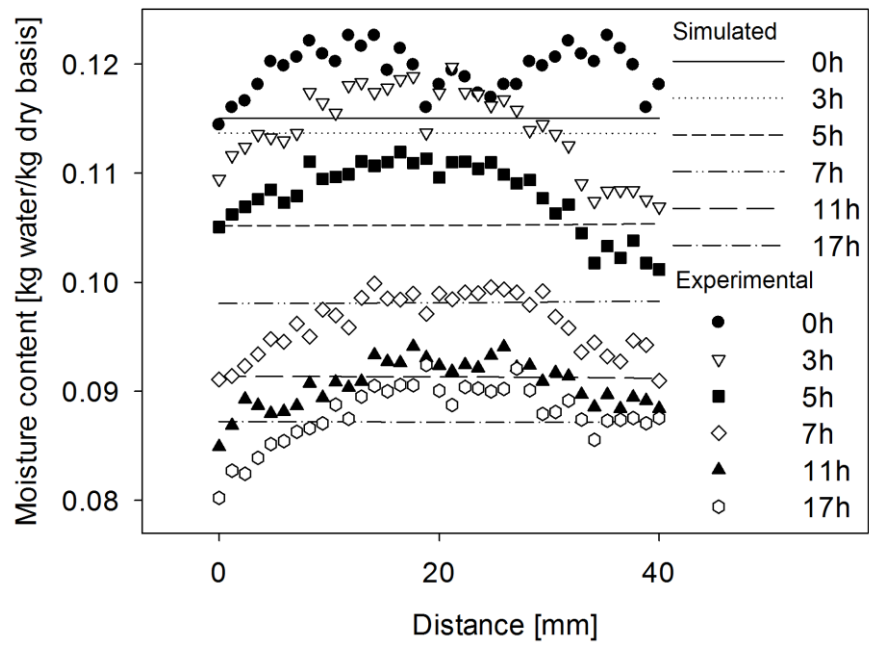


b)

Figure 4

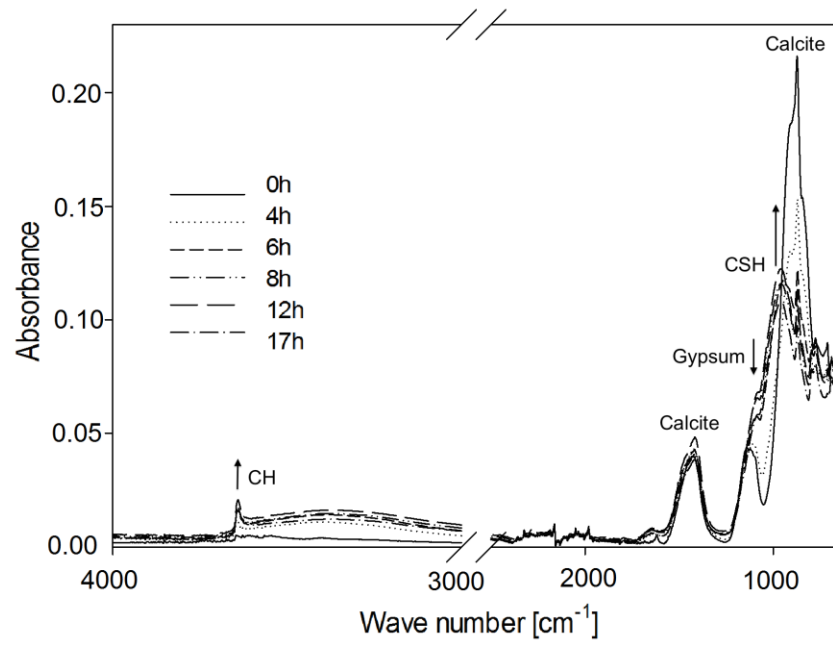


a)

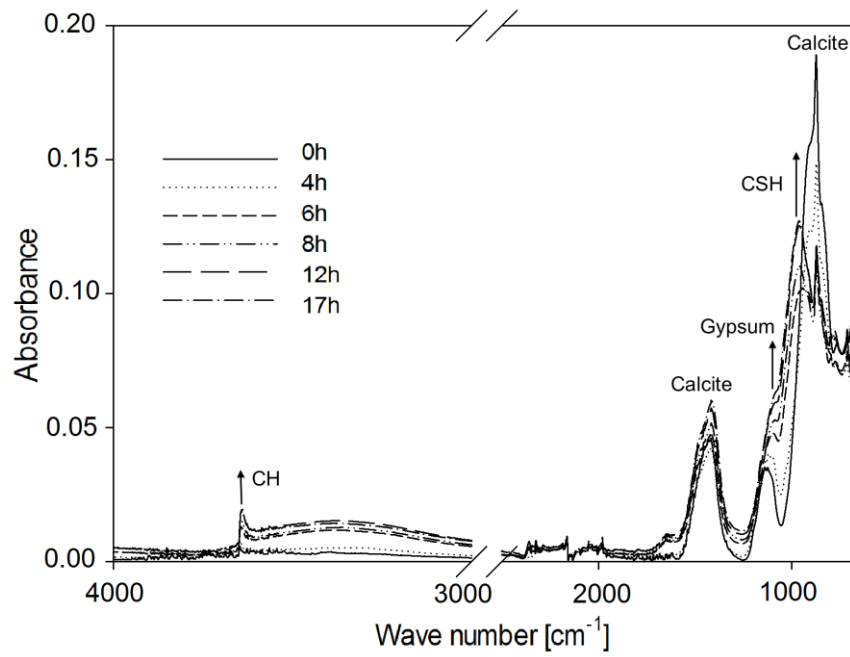


b)

Figure 5



a)



b)

Figure 6

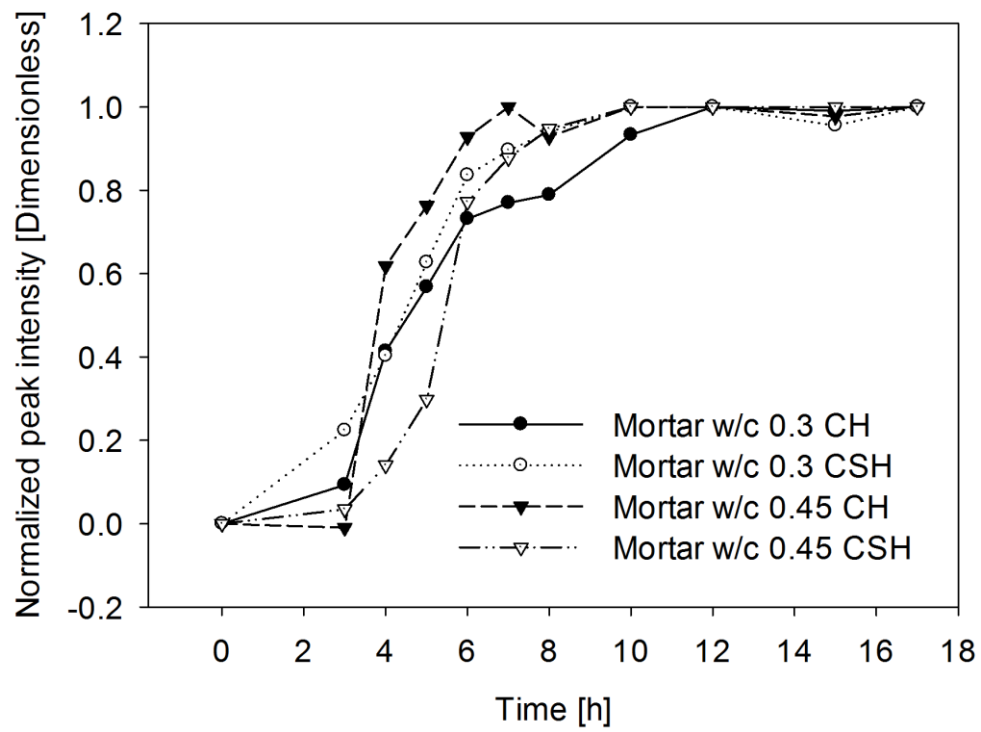


Figure 7

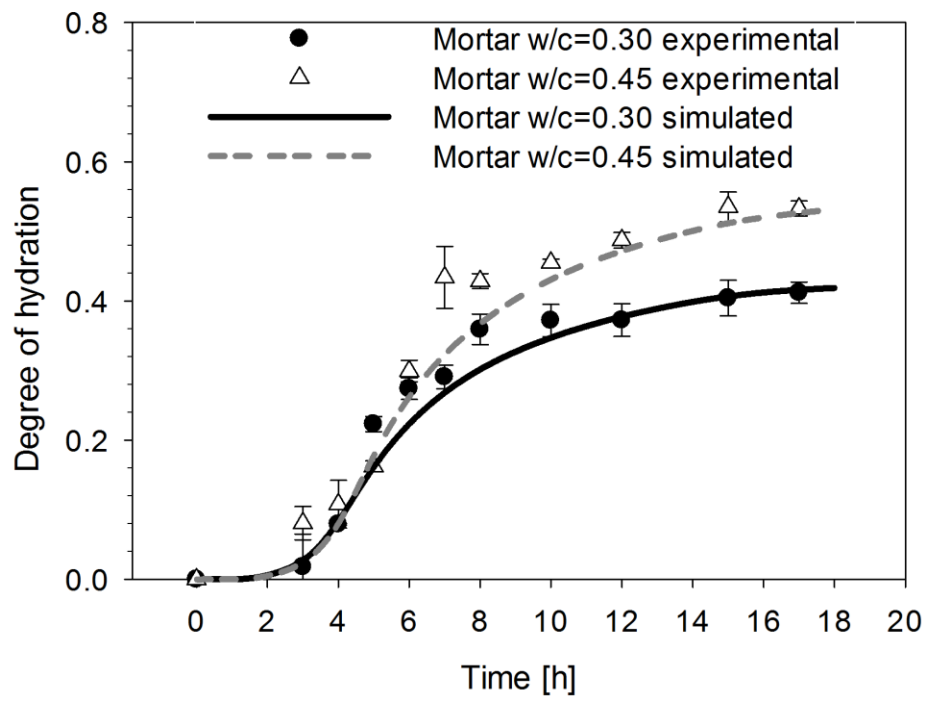


Figure 8

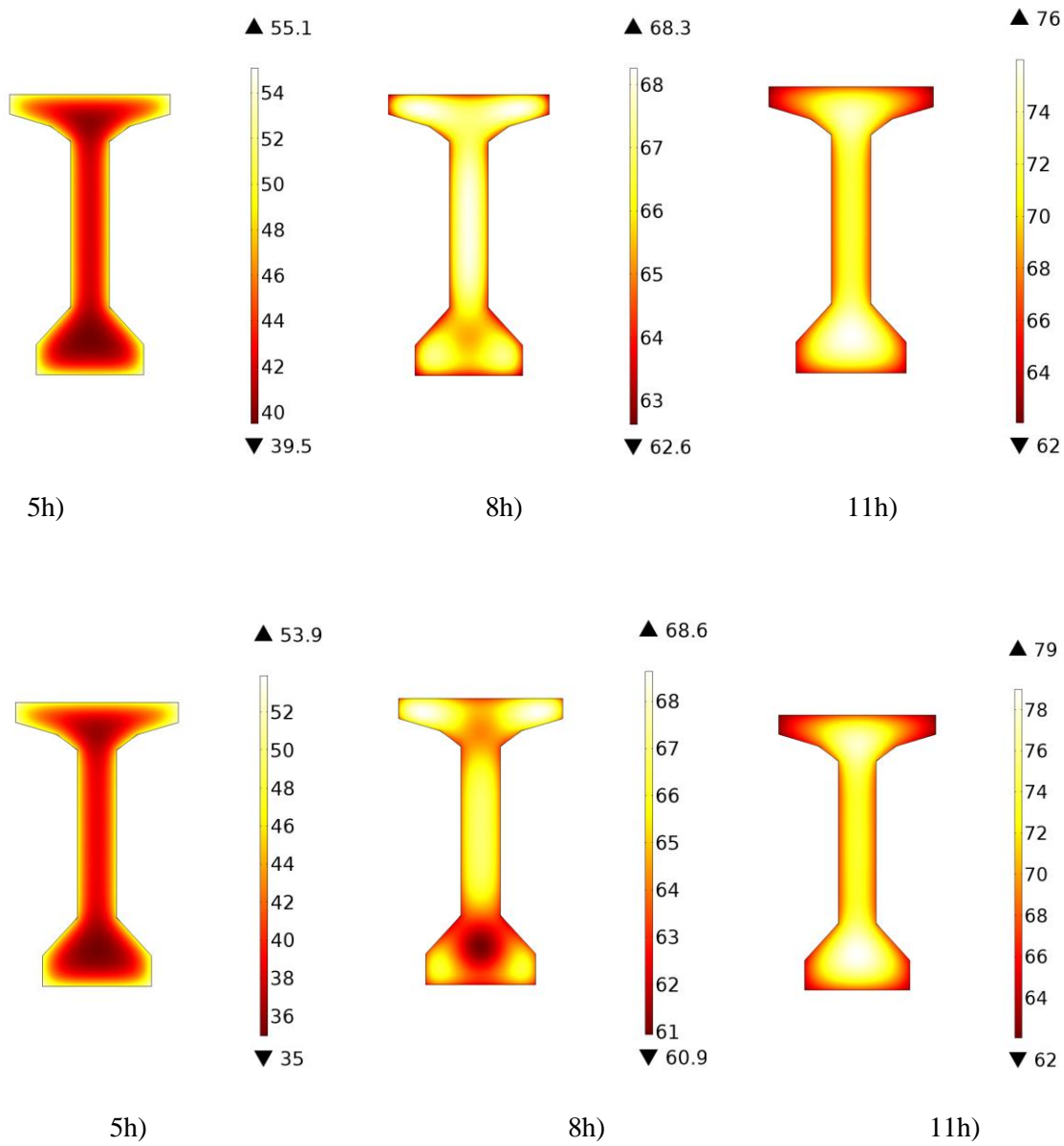
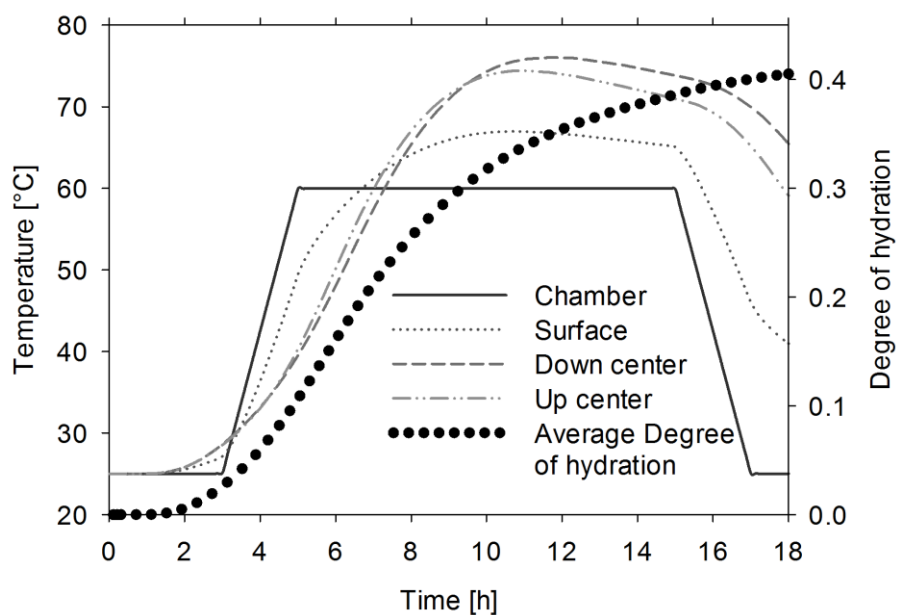
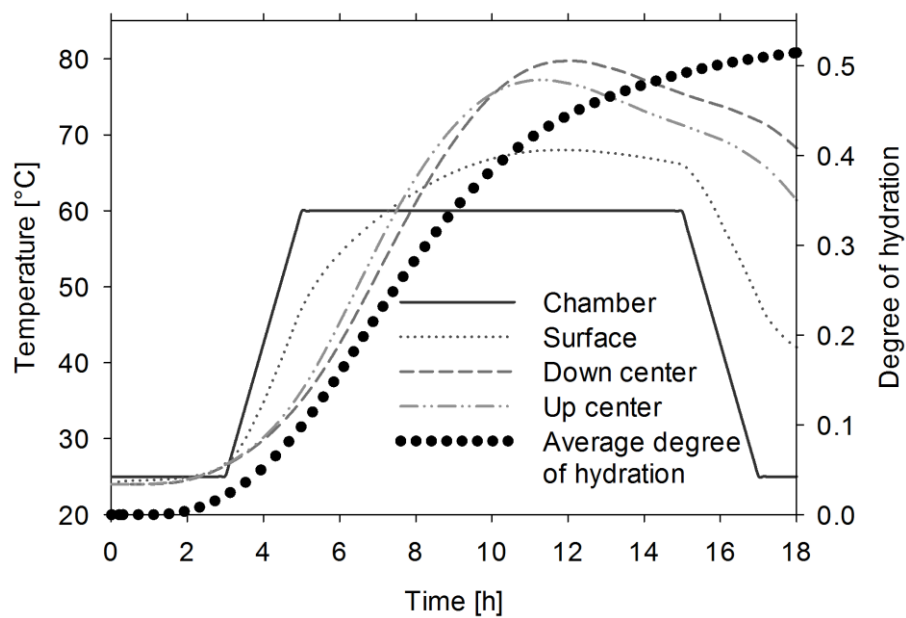


Figure 9

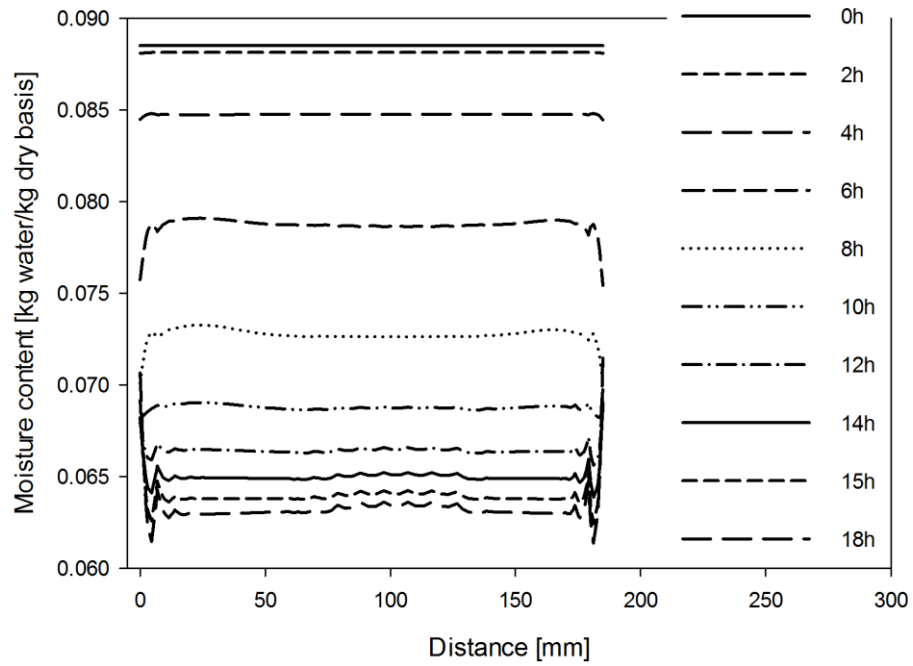


a)

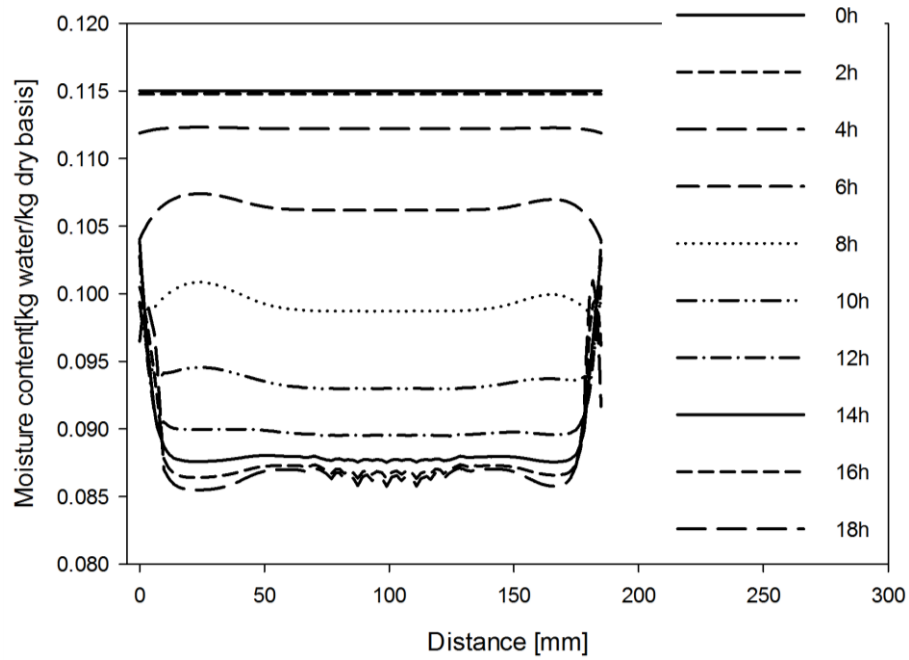


b)

Figure 10



a)



b)

Figure 11

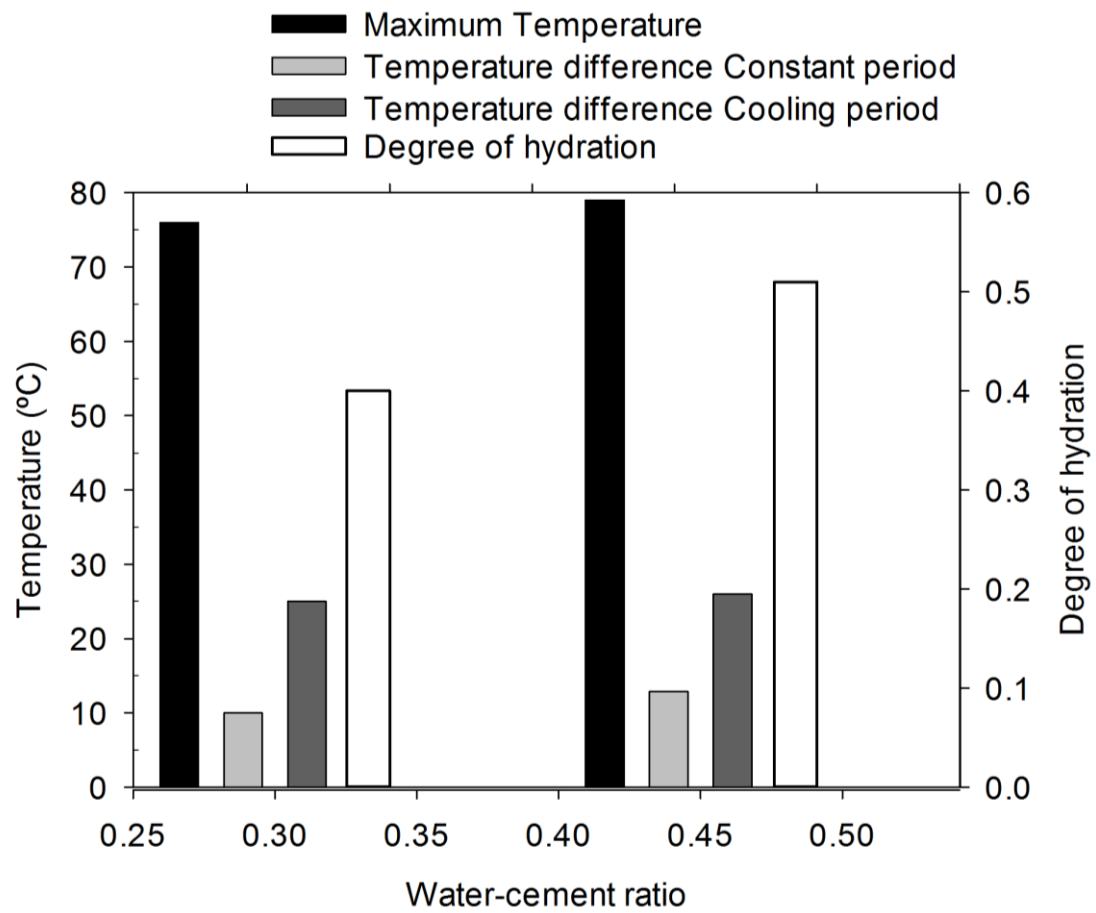


Figure 12

Table 1. Portland cement chemical composition

Oxide	% Mass	Oxide	% Mass
CaO	62.5	Mn ₂ O ₃	1.5
SiO ₂	21.5	K ₂ O	1.5
Al ₂ O ₃	4.5	SO ₃	1.0
MgO	2.5	Na ₂ O	0.7
TiO ₂	2.0	P ₂ O ₅	0.5
Fe ₂ O ₃	1.8		
LOI	2.5		

Table 2. Mixture proportions for 1 m³ of mortar

	$w/c = 0.30$	$w/c = 0.45$
Cement (kg)	648	521
Water (kg)	194	235
Silica sand (kg)	1548	1548

Table 3. Summary of the main equations in the model

Eq. number	Conservative equation	e	U	J	Q
(2)	Equivalent time	1	t_e	0	$\exp\left[\frac{E}{R}\left(\frac{1}{T_r} - \frac{1}{T}\right)\right]$
(3)	Maturity	1	α	0	$\frac{dt_e}{dt} \cdot \frac{\alpha_u \beta}{t_e} \left(\frac{\tau}{t_e}\right)^\beta \exp\left[-\left(\frac{\tau}{t_e}\right)^\beta\right]$
(4)	Heat	$r_s C_p$	T	$k \cdot \nabla T$	$\frac{dt_e}{dt} \cdot \frac{H_u \alpha_u \beta}{t_e} \left(\frac{\tau}{t_e}\right)^\beta \exp\left[-\left(\frac{\tau}{t_e}\right)^\beta\right]$
(5)	Mass	r_s	w	$r_s \times D_l \frac{\nabla w}{\nabla x} + D_v \frac{\nabla h}{\nabla x}$	$-\rho_s \cdot M_f^{cem} \cdot w_n \frac{d\alpha}{dt}$

Table 4. Initial and boundary conditions for the model $w/c = 0.30$ and $w/c = 0.45$

Eq. number		Surface g	Initial condition
(7)	Equivalent time	0	$t=0$ then $\alpha=0$
(8)	Maturity	0	$t=0$ then $t_e=0$
(9)	Heat	$h_c \times (T_{ext} - T) + l_{vap} \times h_m \times (P_{Vext} - P_V)$	$t=0$ then $T=24\text{ }^\circ\text{C}$
(10)	Mass	$h_m \times (P_{Vext} - P_V)$	$t=0$
			$w/c=0.3$ then $w_i=0.0880$
			$w/c=0.45$ then
			$w_i=0.1105$

Table 5 Constitutive equations and variables for the model. Data for mortars with $w/c = 0.30$ and $w/c = 0.45$ is provided.

Eq. number	Variable	w/c=0.30		w/c=0.45		Source
Maturity equation and equivalent time						
	T_r	23°C		23°C		[11]
	α_u	0.50		0.69		[11]
	τ	10.09 h		12.75 h		[11]
	β	0.98		0.898		[11]
	E	For 23 °C	32800 (J/mol)	For 23 °C	27400 (J/mol)	[16] [6]
		For 60 °C	25700 (J/mol)	For 60 °C	27400 (J/mol)	
Mass conservation equation						
	D_v	0.0155 g/(m*d)		0.0004 g/(m*d)		[27]
(11)	$D_l =$	b exp(cw)		b exp(cw)		[27]
		b=0.0055		b=0.0033		
		c= 144		c= 155		
	r_s	2390 kg/m³		2304 kg/m³		[16]
	w_n	0.23055 g water/g cement				[17]
	M_f^{cem}	0.271		0.229		[11]
Heat conservation equation						
	k	2.9 W/(m·K)		2.8 W/(m·K)		[16]
(12)	C_p^{CemBM}	$4180M_f^{water} + 2090M_f^{boundwater} + 722.5M_f^{cem} + 635.3M_f^{SilicaSand}$				[21]
(13)	l_{vap}	$\lambda_{vap}=2500000+1859TJ/(kg\cdot K)$				[6]
	h_m	5x10 ⁻³ g/(m²·h)		10x10 ⁻³ g/(m²·h)		[20]
	h_c	36 W/(m²·K)				[20]

Table 6 Characteristic wavelengths of the infrared spectra [24]

Assignment		Functional group	Movement	FTIR band (cm ⁻¹)
O-H (in Portlandite)	Ca(OH) ₂	O-H	O–H stretching mode in Portlandite, Ca(OH) ₂	3641
SiO ₄ (in C-S-H)	CaO · SiO ₂ · H ₂ O	SiO ₄	Si–O stretching and Si–OH bending	965
C-O (in CaCO ₃)	CaCO ₃	C–O		1418, 873